**Ninth International Conference on
Computational Fluid Dynamics (ICCFD9),
Istanbul, Turkey, July 11-15, 2016** **ICCFD9-2016-288**

Efficient and accurate PLIC-VOF techniques for numerical simulations of free surface water waves

Bülent Düz[1,4], Mart J.A. Borsboom[2], Arthur E.P. Veldman[3], Peter R. Wellens[2],
Rene H.M. Huijsmans[4]

[1] Maritime Research Institute (MARIN), Wageningen, The Netherlands
[2] Deltares, Delft, The Netherlands
[3] Institute for Mathematics and Computer Science,
University of Groningen, Groningen, The Netherlands
[4] Department of Ship Hydromechanics and Structures,
Delft University of Technology, Delft, The Netherlands

Corresponding author: b.duz@marin.nl

Abstract: In this paper the attention is focused on the effect of various VOF methods on efficient and accurate simulation of free surface water waves. For this purpose, we will compare several VOF methods in numerical simulations of propagating waves where strong nonlinear behavior is dominant in the flow. Comparisons and discussions will be provided to underline the significance of free surface modeling on the accuracy of wave propagation.

Keywords: Free surface modeling, PLIC-VOF techniques, Wave propagation, Spurious wave damping, MACHO and COSMIC schemes.

1 Introduction

Free surfaces or interfaces between immiscible fluids are broadly featured in many processes in modern industry as well as within the human body and in the environment we live in. In addition to various computational modeling challenges that the free surface flows present, the mere existence of a free surface poses some difficulties. On the one hand the solution region changes as the free surface evolves, and on the other hand, the motion of the free surface is in turn determined by the solution. Changes in the solution region include not only changes in size and shape, but in some cases, may also include the coalescence and break up of regions (i.e., the loss and gain of free surfaces). During these processes it is important to keep the free surface sharp and well-defined, and evolve it without smearing, dispersing or wrinkling. This is a critically significant task in order to achieve an accurate solution to the overall physical problem.

Numerical methods for modeling free surfaces have been a popular subject for several decades among researchers from various fields of science. This resulted in various types of strategies with different theoretical backgrounds that can robustly and efficiently represent evolving and topologically complex free surfaces. It is a quite challenging effort to cite all major developments due to the large volume of the existing literature. Below we give a brief survey of these strategies and refer interested readers to [1] and [2] for more extensive surveys.

In marker methods massless markers or tracers are used on a fixed mesh to track fluid volumes in the entire flow domain (volume markers) or to track exactly the location of the interface (surface markers). The positions of the markers are updated using the underlying velocity field in a Langrangian fashion. One of the earliest works in this field goes back to [3] where massless markers were used in the entire flow domain, the marker-and-cell method (MAC). In following works markers were used only on the interface. This resulted in a significant reduction in computer time and storage, and also provided the explicit location of the interface. Over the years [4], [5] and [6], among others, made important contributions to this idea.

In the level-set method introduced by [7] a continuous level-set function is used to track the motion of an interface. The interface is represented as the zero level set of this signed distance function. Inside one of the fluids the function takes a positive value, and in the other fluid it takes a negative value. The level-set function moves with the fluid, and therefore evolves according to a simple transport equation. Even though it is conceptually simple as well as easy to implement, issues with mass conservation were reported in early implementations especially when the interface undergoes large deformations. [8] and [9] proposed strategies to improve the mass conservation property of the level-set method.

In [10] a powerful family of constrained interpolation profile (CIP) methods was proposed. The CIP method was initially presented by [11], and the abbreviation then stood for *cubic interpolated pseudo-particle*. Over the years the method has evolved, its name has changed but the abbreviation stayed the same. Nonetheless it has been successfully applied to various multi-phase flows; see [10]. The strength of this method stems from the strategy that it uses the primitive variables and their derivatives as a set of dependent variables. For the first group the conservation equations are used and for the second group the corresponding derivatives of these equations are used. The recent version of the method guarantees exact mass conservation, and results in a low dispersion error. The reader is referred to the aforementioned and other publications from these researchers for further discussions on the CIP method.

Before going into the details of the volume-of-fluid (VOF) method which constitutes the backbone of the present work, it is important to note that there are other methods used for interface tracking/capturing in interfacial and free surface flows. Among these methods are phase-field [12] and [13], continuum advection [14], point-set [15], Langrangian [16] and [17], and moment-of-fluid (MOF) [18].

Volume-of-fluid (VOF) methods have been successfully used in computational fluid dynamics (CFD) simulation of interfacial and free surface flows for several decades since the introduction by [19]. Typically, the VOF approach presents a model based on a scalar indicator function to transport the fluid from one cell to another on a fixed computational mesh using the underlying velocity field. This function is characterized by the volume fraction F occupying one of the fluids within each cell. If a cell is completely filled with one fluid, the volume fraction takes the value of 1, and 0 if only the second fluid is present. The values between these two limits indicate the presence of the interface or free surface. In the VOF approach, the volume fraction field is the only available and required information representing the interface profile. Therefore, if the explicit location of the interface is needed, special algorithms have to be applied to attain an approximate reconstruction of the interface by exploiting the volume fraction distribution of the neighboring cells in a compact stencil.

In the VOF technique, the volume fraction field is propagated by solving a scalar transport equation. Discretization of the transport equation with an accurate numerical method is critical for not only the conservation of mass but also evolving the interface without smearing, dispersing or wrinkling it. This basically constitutes the principal drawback of the VOF approach, especially considering the fact that the discrete volume fraction field is not smoothly distributed at the interface (on the contrary it displays sharp discontinuous changes between 0 and 1). In this regard, conventional convective differencing schemes, such as upwinding, are unable to maintain a well-defined interface due to numerical diffusion, even if they do not violate the boundedness of the solution ($0 \leq F \leq 1$) through the sufficient boundedness criterion. In order to resolve the interface while modeling fluid flow behaviors such as large deformation, interface rupture and coalescence in a natural fashion, researchers have developed numerous techniques within the VOF function framework. They can be classified into three categories: donor-acceptor formulation, high resolution differencing schemes and line techniques (explicit geometrical reconstruction of the interface).

In the donor-acceptor formulation, the volume fraction values of the downwind and upwind of a flux boundary are used to estimate the amount of volume fraction transported through that boundary during a time step. These volume fraction values are used to predict the orientation of the interface when computing the flux volume. Hence, local interface reconstruction is not essentially needed. However, the inclusion of downwind information generally violates the boundedness criterion causing unphysical overshoots and undershoots. In order to ensure boundedness, several improvements have been incorporated into the donor-acceptor formulation, such as *controlled downwinding*. This idea established the structure for the derivation of the well-known VOF method by [19]. To take a more in-depth look at the donor-acceptor formulation, see [20, 21, 22, 23].

High resolution differencing schemes utilize the idea of implementing a higher order or blended differencing scheme to approximate the transport equation. These schemes outperform the first-order upwind scheme in terms of accuracy, and the second-order central difference scheme in terms of stability; see [24]. However, they fail to satisfy the boundedness criterion of the volume fraction values provoking overshoots and undershoots in regions where steep gradients of the flow variables appear along with the high local Peclet number. To surpass this shortcoming, many techniques have been proposed. For a discussion concerning high resolution schemes, see [25], [23], and [26].

In line techniques, the interface is locally reconstructed and corresponding volume fluxes are computed to preserve the sharp profile of the interface. Based on the volume fraction values of the neighboring cells, the orientation and location of the interface in a cell can be calculated in a piecewise constant, piecewise linear or piecewise parabolic fashion. The resulting reconstructed interface is not necessarily continuous, but a rather discontinuous chain of discrete line segments. However, from piecewise constant to piecewise parabolic reconstruction, the discontinuities at the cell boundaries decrease substantially, see [27].

The Simple Line Interface Calculation (SLIC) by [28] was the cornerstone of the geometric interface reconstruction techniques. Here the reconstructed interface is a straight line parallel to one of the spatial directions. For the reconstruction, only the volume fraction values of the neighboring cells along a coordinate direction are taken into account in a 3×1 block of cells. Therefore, the interface has a different representation depending on the coordinate direction considered for the reconstruction. [29] further improved this reconstruction concept by evaluating the volume fraction information in a 3×3 block of cells, nevertheless his version also yields different fluid distributions for each sweep direction. In any case, the extension of SLIC to 3D is straightforward. In addition to first-order accuracy, SLIC also results in the shedding of many isolated blobs of *flotsam* and *jetsam* by artificially breaking up the interface [1].

Among the three approaches, the piecewise linear reconstruction is nowadays the most popular approach, and the methods which fall into this category are usually referred to as Piecewise Linear Interface Calculation- or Construction (PLIC) methods. In this approach, the interface is reconstructed by oblique or piecewise linear line segments (or plane segments in 3D). As the reconstruction is performed in a multidimensional manner, the interface does not have a different representation depending on the sweep direction. After [30] and [31] designed first PLIC methods, researchers have made a significant effort developing methods to achieve second-order accuracy at reasonable computational cost. See [18, 32, 33] for a survey of PLIC methods.

In Piecewise Parabolic Interface Calculation (PPIC) by [27], the interface is approximated by an arbitrarily rotated parabola. Hence, the interface is modeled in a more natural way especially in high curvature regions. Moreover, the local curvature of the interface is directly available, which is especially required for modeling the surface tension force acting on the interface. PPIC is inherently third-order accurate if the interface is sufficiently smooth. Unfortunately, this method is only available in 2D.

In the VOF context, to advect the volume fraction field in time, the following transport equation is solved,

$$\frac{\partial F}{\partial t} + \mathbf{u} \cdot \nabla F = 0, \tag{1}$$

where $\mathbf{u} = (u, v, w)$ denotes the fluid velocity vector, and $\nabla = (\partial/\partial x, \partial/\partial y, \partial/\partial z)$ is the gradient operator. Assuming a solenoidal velocity field (incompressible flow) modeled by $\nabla \cdot \mathbf{u} = 0$, Eq. (1) can alternatively take the form:

$$\frac{\partial F}{\partial t} + \nabla \cdot (\mathbf{u}F) = 0. \tag{2}$$

Equation (2) can be solved using either an unsplit advection or an operator split advection scheme. Although both strategies have been successfully applied in simulation of interfacial flows, direction split advection schemes are more common in VOF methods due to ease of implementation. Treating individual velocity components to compute 1D fluxes for a sequence of updates in each spatial direction is easier compared to treating velocity components acting in all directions to compute multidimensional fluxes using inherently difficult geometric tasks. However, operator splitting has a strict limitation: it is applicable only within structured mesh environments. The transport problem in the VOF method is analyzed in more detail in Section 3.

Several attempts have also been made to benefit from advantages of various strategies through coupling them in a hybrid method. [34] developed a coupled level-set/VOF method (CLSVOF) in order to exploit the favorable features of both the VOF and level-set methods. Here the contribution of the level-set method is to keep a fine description of the geometrical properties of the interface, while that of the VOF method is to minimize mass loss, see [35] for a further discussion on this coupling. Recently [36] proposed a hybrid level-set/moment-of-fluid method (CLSMOF) which uses information from the level set function, volume of fluid function, and reference centroid.

The PLIC-VOF technique in this work has been incorporated into a numerical method called ComFLOW. ComFLOW was initially developed to simulate one-phase flow. Later, implementation of the method was extended to a wider class of problems after improving the method to model two-phase flows [37] and [38]. Simulation of sloshing on board spacecraft [39], [40], [41]; medical science [42], [43]; μ-gravity biology applications [44]; engineering problems in maritime and offshore industry [45], [46], [47], [48], [49], and [50] are among those where ComFLOW has been generally used. The reader is referred to [51, 52] and the ComFLOW website (www.math.rug.nl/∼veldman/comflow/comflow.html) for an overview of the current status of the method.

Since the CFD tool ComFLOW is currently in use for practical applications especially in 3D, the required VOF method must be computationally cheap, robust and easily applicable while retaining a reasonable accuracy for representing complex free surfaces. In each section below, after shortly explaining the corresponding subject, we will keep these criteria in mind while choosing or implementing a numerical technique. As one of the main application areas of ComFLOW is wave impact loading on offshore structures and coastal construction, accurate simulation of propagating free surface waves with reasonable computational resources is of critical importance. In that respect, we will pay particular attention to the performance of the methods in this problem. The layout of the rest of the paper is as follows. In Section 2, a brief introduction to piecewise linear interface reconstruction will be given. Section 3 discusses interface advection along with geometrical flux computation. Section 4 presents results from a series of test cases which includes advection tests, and an application example where VOF methods are used in ComFLOW to simulate two wave cases, a small-amplitude wave with low steepness and a relatively large-amplitude wave with high-steepness. We end the paper with conclusions in Section 5.

2 Interface reconstruction

The interface reconstruction is the first stage of a typical VOF method. In the PLIC approach, the interface in each cell is approximated by a line (or a plane in three dimensions). Within each cell, the approximated interface can be defined by the equation:

$$\mathbf{m} \cdot \mathbf{x} = m_x x + m_y y + m_z z = \alpha, \tag{3}$$

where $\mathbf{m}$ is the local surface normal, $\mathbf{x}$ is the position vector of a point on the interface and α is a constant which is related to the shortest distance from the origin of the cell. Essentially, the interface reconstruction involves two procedures: the determination of $\mathbf{m}$ and α. In this section, we will investigate the algorithms designed to obtain $\mathbf{m}$, and the determination of α is explained in Section 2.1. For a given discrete volume fraction field, $\mathbf{m}$ in each cell is usually calculated using the data in a compact neighborhood of the cell considered. However, since the discrete volume fraction field is not smoothly distributed at the interface, computation of $\mathbf{m}$ with high accuracy can be complicated and expensive. Modeling the interface by simply adopting a piecewise linear representation does not always result in a second-order approximation since the accuracy of the reconstruction depends critically on the calculation of the normal. Furthermore, the size of the discontinuities at the cell boundaries are also sensitive to the calculation of the normal. As the grid resolution and the accuracy of the calculation of the normal increase, the discontinuities decrease. However, in general, truly second-order reconstruction methods tend to require high computational effort especially for three-dimensional implementations. Computational costs increase even further when these methods are used in combination with operator split advection techniques because the resulting algorithm will demand a number of reconstruction sweeps at each time step.

Among many techniques that are available in the literature, we will consider four methods: Parker and Youngs' method (P&Y) [53], the least squares gradient (LSG) technique by [54], the Mixed Youngs-centered (MYC) implementation of [55] and the efficient least squares VOF interface reconstruction algorithm

(ELVIRA) by [56]. The ELVIRA scheme by [56] was originally proposed in 2D. For the 3D implementation, we will consider the approach by [57]. We will later demonstrate that the level of accuracy of some of these methods are satisfying for the problems we typically encounter. In addition, all the four schemes are mathematically simple, non-iterative and involve a small number of algorithmic tasks. Therefore, implementing these methods require a modest amount of programming work, and the result can be achieved in an economical manner.

2.1 Computation of the plane constant

Once the normal vector is known, the planar interface within the cell is located so that local volume conservation is satisfied. In other words, the resulting plane should pass through the cell in such a way that the truncated volume lying below the plane is equal to the exact material volume in that cell. In three dimensions, the intersection of a plane with a cube is an inscribed, irregular polygon with one of four basic shapes which have 3 to 6 intersection points, as shown in Fig. 1.

As Eq. (3) suggests, the location of the planar interface results from the computation of α. With the available knowledge of the normal vector $\mathbf{m}$ and the volume fraction F within the cell, α can be calculated either iteratively or analytically.

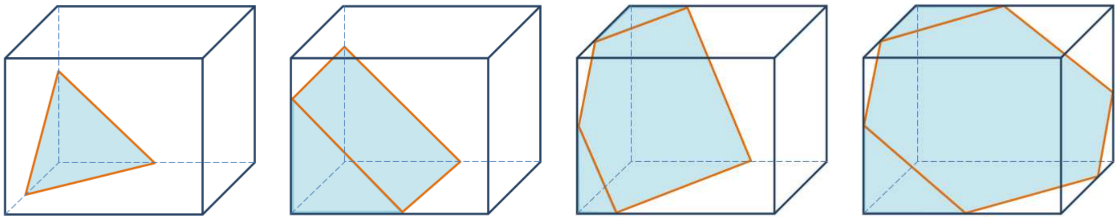
(a) 3-sided polygon (b) 4-sided polygon (c) 5-sided polygon (d) 6-sided polygon

Figure 1: Possible candidates of irregular polyhedron within a cubic mesh cell.

Several approaches have been proposed for computation of plane constant, which can be classified as analytical and iterative methods. [54] proposed the use of Brent's scheme as in [58] which includes a combination of bisection and inverse quadratic interpolation methods to find a near-optimal next guess for α. They also report that Newton's method does not guarantee convergence. An algorithm based on secant and bisection methods is given in [59].

Analytical relations for the forward and inverse problems were presented in [60, 61] (forward problem refers to finding the volume fraction for a given α and inverse problem refers to finding α given the volume fraction). They report that analytical relations are computationally cheaper than a fast root-finding technique. In a recent study, [62] reports that the forward and inverse routines by [60] have been well tested and are free from inconsistencies which may occur due to round-off errors in limiting cases. Analytical relations by [60] were also used in this work.

3 Interface advection

After the orientation and location of the planar interface are determined, the volume fraction field is advected in time via Eq. (2). This is the second stage of a VOF method. Algorithms for the transport problem may generally be divided into two categories: unsplit schemes and operator split schemes. In operator splitting, the transport of the volume fraction field is realized by considering sequential updates along each direction with calculating one dimensional fluxes by treating only one velocity vector component in each update. This inherent feature makes operator splitting applicable only within structured mesh environments. After advancing the interface along each coordinate direction, intermediate volume fraction values are computed. As a result, three consecutive updates are required to transport the interface to the next discrete time level in three dimensions, $F^n \rightarrow F^* \rightarrow F^{**} \rightarrow F^{n+1}$, which also necessitates at least three interface reconstruction sweeps based on the corresponding intermediate volume fraction fields. Additionally, the sequence of updates in each direction must be changed in order to avoid, or at least minimize, asymmetries caused by the operator splitting; [54], [63]. For this purpose, six possible permutations of the sweep sequence in three directions need to be realized; [64], [63]. In unsplit advection, however, fluxes are calculated using the velocity vector components acting in all directions. Therefore, several neighboring cells may contribute to a multidimensional flux volume across a mesh cell face over a time step which is truncated by an arbitrarily-oriented planar interface. This procedure constitutes the fundamental bottleneck of unsplit advection since the resulting multidimensional flux volume may have a very complex geometry. Once multidimensional flux volumes through each mesh cell face are determined, the interface is propagated along all coordinate directions in a single update, $F^n \to F^{n+1}$, which entails only one interface reconstruction sweep. This clearly brings a significant advantage in terms of computational costs. Compared to unsplit advection, operator splitting is more common among researchers and well-documented.

Irrespective of the transport strategy, an advection method should be *mass conserving*, *shape preserving* and satisfy the *constancy condition*. The total mass must be conserved without a posteriori numerical treatment. The constancy condition requires that an initially uniform scalar field governed by Eq. (2) should remain uniform in a divergence free velocity field. A shape preserving advection scheme does not generate unphysical undershoots or overshoots, i.e., the volume fraction field must always be bounded everywhere, $0 \leq F \leq 1$; see [63] for an in-depth discussion. Unfortunately, it is difficult to design an advection scheme which satisfies all criteria simultaneously. Typically shortcomings of various advection schemes are compensated through *ad hoc* workarounds. For example, when there is an overshoot and/or undershoot in volume fraction values, excess values are clipped or dispensed over several neighboring cells, e.g., [65] present a mass redistribution algorithm to account for overshoots and undershoots without violating mass conservation, [54] also search for and conservatively redistribute any volume fraction excess values ($F < 0$ and/or $F > 1$), [66] only mention such a local redistribution procedure, and [49] uses a local height function to restore mass conservation. When mass is redistributed, also momentum is likely to change. Hence, although mass conservation is repaired, momentum conservation is lost. Another approach to circumvent this difficulty is to combine the advection method with a flux correction scheme, e.g., [67] introduces such a scheme which is embedded into the procedure for the computation of the flux volume. [68] also discusses this subject and presents and idea to overcome this problem which is based on the concept of allowing volume of a cell to change effectively during each one-dimensional sweep of advection. He mentions that even after this measure small round-off errors can accumulate and affect the boundedness of the volume fraction field later in the simulation. For discussions about the useful attributes which an advection scheme should retain, see [63], [69] and [70].

Both strategies for advection have been investigated by many researchers. In this work, we restrict the discussion regarding advection methods to operator split schemes. For unsplit advection techniques, the reader is referred to the works by, e.g., [71], [54], [72], [73], [56], [33], and [74].

In [63] two operator split advection methods were introduced which, to the best knowledge of the authors, have not been used within the context of interfacial or free surface flows. The schemes are Multidimensional Advective-Conservative Hybrid Operator (MACHO) and Conservative Operator Splitting for Multidimensions with Inherent Constancy (COSMIC). In 2D, the MACHO and COSMIC schemes take the following form:

- the 2D MACHO scheme:

$$
\begin{aligned}
F^* &= F^n - \Delta t \frac{\partial u F^n}{\partial x} + \Delta t F^n \frac{\partial u}{\partial x}, \\
F^{n+1} &= F^n - \Delta t \left(\frac{\partial u F^n}{\partial x} + \frac{\partial v F^*}{\partial y} \right),
\end{aligned}
\tag{4}
$$

- the 2D COSMIC scheme:

$$\begin{aligned}
F^X &= F^n - \Delta t\frac{\partial uF^n}{\partial x} + \Delta t F^n\frac{\partial u}{\partial x},\\
F^Y &= F^n - \Delta t\frac{\partial vF^n}{\partial y} + \Delta t F^n\frac{\partial v}{\partial y},\\
F^{n+1} &= F^n - \Delta t\left[\frac{\partial}{\partial x}\left(u\frac{F^n+F^Y}{2}\right) + \frac{\partial}{\partial y}\left(v\frac{F^n+F^X}{2}\right)\right].
\end{aligned} \tag{5}$$

Similar to typical operator split methods, MACHO requires the direction of propagation to be alternated at each time step to reduce directional bias. This, however, is not required by COSMIC because of its inherent symmetric form. By considering the transverse contribution to each flux in (5), COSMIC maintains multidimensional stability. On the other hand, the COSMIC scheme demands one more reconstruction sweep per time step in 2D than any other operator split advection schemes mentioned in this work. In 3D, the increase in computational cost becomes more significant with COSMIC. MACHO and COSMIC can be written as the following in 3D:

- the 3D MACHO scheme:

$$\begin{aligned}
F^* &= F^n - \Delta t\frac{\partial uF^n}{\partial x} + \Delta t F^n\frac{\partial u}{\partial x},\\
F^{**} &= F^* - \Delta t\frac{\partial vF^*}{\partial y} + \Delta t F^*\frac{\partial v}{\partial y},\\
F^{n+1} &= F^n - \Delta t\left(\frac{\partial uF^n}{\partial x} + \frac{\partial vF^*}{\partial y} + \frac{\partial wF^{**}}{\partial z}\right),
\end{aligned} \tag{6}$$

- the 3D COSMIC scheme:

$$\begin{aligned}
&F^X = F^n - \Delta t\frac{\partial uF^n}{\partial x} + \Delta t F^n\frac{\partial u}{\partial x}, \quad F^Y = F^n - \Delta t\frac{\partial vF^n}{\partial y} + \Delta t F^n\frac{\partial v}{\partial y},\\
&F^Z = F^n - \Delta t\frac{\partial wF^n}{\partial z} + \Delta t F^n\frac{\partial w}{\partial z},\\
&F^{XY} = F^Y - \Delta t\frac{\partial uF^Y}{\partial x} + \Delta t F^Y\frac{\partial u}{\partial x}, \quad F^{YX} = F^X - \Delta t\frac{\partial vF^X}{\partial y} + \Delta t F^X\frac{\partial v}{\partial y},\\
&F^{XZ} = F^Z - \Delta t\frac{\partial uF^Z}{\partial x} + \Delta t F^Z\frac{\partial u}{\partial x}, \quad F^{ZX} = F^X - \Delta t\frac{\partial wF^X}{\partial z} + \Delta t F^X\frac{\partial w}{\partial z},\\
&F^{YZ} = F^Z - \Delta t\frac{\partial vF^Z}{\partial y} + \Delta t F^Z\frac{\partial v}{\partial y}, \quad F^{ZY} = F^Y - \Delta t\frac{\partial wF^Y}{\partial z} + \Delta t F^Y\frac{\partial w}{\partial z},\\
&F^{n+1} = F^n - \Delta t\left[\frac{\partial}{\partial x}\left(u\frac{2F^n+F^Y+F^Z+F^{YZ}+F^{ZY}}{6}\right)\right.\\
&\qquad + \frac{\partial}{\partial y}\left(v\frac{2F^n+F^X+F^Z+F^{XZ}+F^{ZX}}{6}\right)\\
&\qquad \left. + \frac{\partial}{\partial z}\left(w\frac{2F^n+F^X+F^Y+F^{XY}+F^{YX}}{6}\right)\right].
\end{aligned} \tag{7}$$

The COSMIC scheme thus entails computing and storing of the three basic one-dimensional updates (F^X, F^Y and F^Z) and the six cross-coupling updates (F^{XY}, F^{YX}, F^{XZ}, F^{ZX}, F^{YZ} and F^{ZY}), all of which are substituted into the single-step explicit update written in conservation form. While MACHO and other operator split algorithms demand three interface reconstruction sweeps at each time step in 3D, COSMIC demands nine interface reconstruction sweeps. Obviously, the symmetry feature of the COSMIC scheme comes at a substantial price. It is noted in [63] that MACHO and COSMIC are not strictly shape preserving under circumstances such as large time steps and deformational velocity fields. However, they add that shape preservation errors are quite small in most practical situations.

Geometric interpretation of the fluxes in MACHO and COSMIC is explained next. For simplicity, let us consider the first relation in Eq. (4) and discretize it in a grid cell such as illustrated in Fig. 2:

$$F^*_{i,j} = F^n_{i,j} - \Delta t \left[\frac{(uF)^n_{i+\frac{1}{2},j} - (uF)^n_{i-\frac{1}{2},j}}{\Delta x_{i,j}} \right] + \Delta t F^n_{i,j} \left[\frac{u^n_{i+\frac{1}{2},j} - u^n_{i-\frac{1}{2},j}}{\Delta x_{i,j}} \right] \tag{8}$$

where $u_{i+\frac{1}{2},j}$ is the velocity component at the center of the right cell face. Suppose that $u_{i+\frac{1}{2},j}$ is positive and divide the cell into two parts, with areas $u_{i+\frac{1}{2},j}\Delta t \Delta y_{i,j}$ on the right and $\left(\Delta x_{i,j} - u_{i+\frac{1}{2},j}\Delta t\right)\Delta y_{i,j}$ on the left. The amount of fluid contained in $u_{i+\frac{1}{2},j}\Delta t \Delta y_{i,j}$ and illustrated as the cross-hatched area will be advected across the right cell face during this time step. If $V^n_{i+\frac{1}{2},j}$ denotes the cross-hatched area corresponding to the initial F^n field, then the approximate volume fraction at the right cell face $F^n_{i+\frac{1}{2},j}$ can be written as

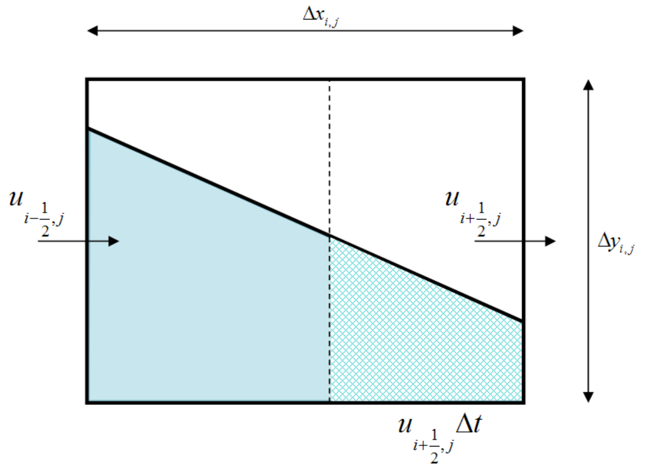

Figure 2: The amount of fluid illustrated as the cross-hatched area crosses the right cell edge in a splitting advection.

$$F^n_{i+\frac{1}{2},j} = \frac{V^n_{i+\frac{1}{2},j}}{u^n_{i+\frac{1}{2},j}\Delta t \Delta y_{i,j}}. \tag{9}$$

In a VOF method, the flux volume can be calculated by exploiting the location of the reconstructed interface. The limits for the flux volume can be stated as $V^n_{i+\frac{1}{2},j} = \min\left(\max\left(V^n_{i+\frac{1}{2},j}, 0\right), u^n_{i+\frac{1}{2},j}\Delta t \Delta y_{i,j}\right)$. After following the same process for the volume fraction at the left cell face and substituting the corresponding relations into Eq. (8), we obtain the following expression for the first step of the MACHO splitting

$$F^*_{i,j} = F^n_{i,j} - \left[\frac{V^n_{i+\frac{1}{2},j} - V^n_{i-\frac{1}{2},j}}{\Delta x_{i,j}\Delta y_{i,j}} \right] + \Delta t F^n_{i,j} \left[\frac{u^n_{i+\frac{1}{2},j} - u^n_{i-\frac{1}{2},j}}{\Delta x_{i,j}} \right]. \tag{10}$$

Now, consider the second step in the MACHO splitting in Eq. (4). Following the same procedure explained above, the discrete form of the second step is given as

$$F^{n+1}_{i,j} = F^{n}_{i,j} - \left[\frac{V^{n}_{i+\frac{1}{2},j} - V^{n}_{i-\frac{1}{2},j}}{\Delta x_{i,j} \Delta y_{i,j}} \right] - \left[\frac{V^{*}_{i,j+\frac{1}{2}} - V^{*}_{i,j-\frac{1}{2}}}{\Delta x_{i,j} \Delta y_{i,j}} \right] \tag{11}$$

where $V^{*}_{i,j+\frac{1}{2}}$ is the flux volume across the north cell face corresponding to the updated volume fraction field F^{*}.

4 Numerical results

The order of accuracy of the reconstruction methods used in this work has been extensively studied by various researchers, see, e.g., [56], [54], [33], [55], [66], and [75]. Therefore, we will not present any static interface reconstruction tests and focus our attention on the kinematic simulations. In all advection tests presented here, velocity fields are defined in such a way that advected fluid bodies return to their initial shapes and locations at the end of the simulation time (often by multiplying the velocity with the Leveque cosine term; [76]). Therefore, a volume fraction distribution at the end of the simulation should be equivalent to the initial volume fraction distribution which can be considered as the exact solution. In order to compare the two distributions, the following error definitions are used

$$E = \sum_{i,j,k} \left| F_{i,j,k} - \tilde{F}_{i,j,k} \right| \Delta x_i \Delta y_j \Delta z_k, \tag{12}$$

$$E = \frac{\sum_{i,j,k} \left| F_{i,j,k} - \tilde{F}_{i,j,k} \right|}{\sum_{i,j,k} F_{i,j,k}}. \tag{13}$$

In both expressions, $F_{i,j,k}$ denotes the exact volume fraction distribution, and $\tilde{F}_{i,j,k}$ denotes the volume fraction distribution obtained by a pair of reconstruction/advection algorithms (simplification to 2D is straightforward). In order to have consistency with previous work, we will switch between the two formulae in the numerical tests.

In total, we have twelve alternative interface-reconstruction/advection combinations. Four interface reconstruction methods that we consider here are: Parker and Youngs' method (P&Y) by [53], least squares gradient (LSG) method by [54], mixed Youngs-centered (MYC) method by [55] and Efficient least squares VOF interface reconstruction algorithm (ELVIRA) by [56]. The ELVIRA scheme by [56] was originally proposed in 2D, hence it will be used in 2D problems. For 3D problems we will consider the ELVIRA scheme by [57]. These interface reconstruction schemes will be combined with the three direction split advection schemes: MACHO and COSMIC by [63], and EI-LE by [66]. However, since the EI-LE scheme is inherently 2D, we will use only MACHO and COSMIC in 3D problems. We will not use every single interface-reconstruction/advection combination in every test. This is required for brevity and compactness.

In addition to the above algorithms, we will show results obtained by using the current VOF implementation in the CFD simulation tool ComFLOW. It employs the classical VOF technique introduced by [19] and a local height function (LHF) to overcome the bottlenecks which originate from this VOF technique such as violation of mass conservation and spurious flotsam and jetsam. For a detailed description of the LHF, see [77]. The combination of this VOF method with the LHF will be referred to as H&N + LHF in the remainder of this chapter.

We will demonstrate the performance of the methods both qualitatively and quantitatively. For qualitative assessment, we will compare graphical results from numerical computations to the exact graphical solution. Figures will illustrate graphical results using $F = 0.5$ isosurfaces. For quantitative assessment, we will analyze the rate of convergence of the methods by using the error metrics given previously. The rate of convergence is computed using

$$O = \frac{\ln \left(E_{\Delta x} / E_{\Delta x/2} \right)}{\ln (2)}, \tag{14}$$

where $E_{\Delta x/2}$ is the error obtained on a grid resolution of $\Delta x/2$, whereas $E_{\Delta x}$ is obtained on a grid resolution of Δx.

We will not focus our attention on the volume conversation since the methods are applied in such a way that volume is strictly conserved. In the numerical tests, we sometimes encountered mild overshoots and undershoots in volume fraction values after advecting the fluid configuration along a coordinate direction. Whenever and wherever this behavior is observed, the local height function is applied to ensure that these excess values are not thrown away.

4.1 Rotation of a slotted disk - 2D

The solid body rotation of the slotted disk problem, often referred to as Zalesak's test [78], has been commonly used by researchers such as [68], [66], [56], [75] and [36]. In this test, a slotted disk with a radius of 0.15, and a slot length of 0.05 and width of 0.25 is initially located at $(0.5, 0.75)$ inside a unit sized box. The rotating flow is generated by a constant vorticity velocity field which is given as:

$$\begin{aligned} u &= (\pi/3.14)\,(0.5 - y)\,, \\ v &= (\pi/3.14)\,(x - 0.5)\,. \end{aligned} \tag{15}$$

According to this configuration, the geometry makes a solid body rotation around the center of the unit sized box, and after 628 time units, it completes one revolution and is expected to return to its initial shape and position.

The velocity field in (15) has the one-dimensional incompressibility, $\partial u/\partial x = 0$ and $\partial v/\partial y = 0$. Therefore, there is no fluid shear introduced by the velocity field, and the interface topology should not change as a result of this advection. Furthermore, since the dilatation term in each one-dimensional update of an operator split advection method vanishes, the advection schemes discussed previously degenerate to similar expressions. Hence, this test becomes useful especially for assessing the convergence rate of reconstruction methods. As a result, only one advection method is considered in combination with several reconstruction algorithms.

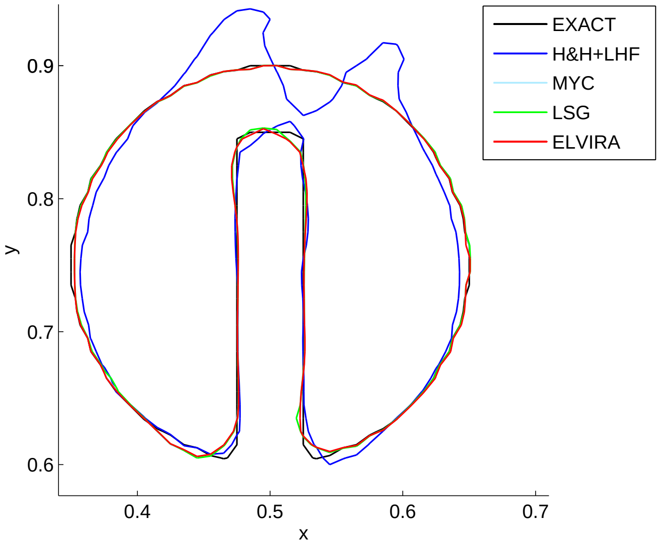

Figure 3: Solid body rotation of a slotted disk in 2D. Numerical results are obtained after one rotation on a 128^2 uniform grid with CFL=0.5. The PLIC methods are combined with the MACHO advection scheme.

The results after one rotation using four methods are illustrated in Fig. 3 in a close-up view. Graphical representation of the exact shape is also shown in black color. The results are obtained by combining the MACHO advection scheme with four reconstruction schemes; P&Y, LSG, MYC and ELVIRA. These methods are also compared to the Hirt and Nichols' VOF combined with the local height function (H&N + LHF). Here the grid size is 128×128, and the CFL number is 0.5.

H&N + LHF performs quite poorly yielding significant distortion on the interface topology even on the smooth segments of the geometry. The results from the MACHO/PLIC schemes are considerably better.

The profiles differ from the exact geometry only in regions with high curvature. We observe that in the corners of the slot, the MACHO/PLIC schemes fail to capture the sharp discontinuities, and smear them out over the neighboring cells. The difference between the PLIC schemes is hardly visible, which suggests that all the methods share similar characteristics in regions of sharp discontinuity.

Mesh	P&Y	MYC	LSG	ELVIRA	H&N+LHF
32^2	1.64×10^{-2}	1.66×10^{-2}	1.68×10^{-2}	1.65×10^{-2}	8.26×10^{-2}
	1.48	*1.48*	*1.50*	*1.49*	*0.99*
64^2	5.88×10^{-3}	5.94×10^{-3}	5.96×10^{-3}	5.87×10^{-3}	4.17×10^{-2}
	1.07	*1.10*	*1.11*	*1.12*	*1.05*
128^2	2.81×10^{-3}	2.78×10^{-3}	2.77×10^{-3}	2.71×10^{-3}	2.01×10^{-2}
	0.99	*1.00*	*1.01*	*1.03*	*1.07*
256^2	1.41×10^{-3}	1.39×10^{-3}	1.38×10^{-3}	1.33×10^{-3}	9.60×10^{-3}

Table 1: Nondimensional error (13) for the solid body rotation of a slotted disk problem. CFL is equal to 0.5. The PLIC methods are combined with the MACHO advection scheme. Rate of convergence (14) is written in italics between mesh entries.

Table 1 shows the nondimensional error (13) for the solid body rotation of a slotted disk problem. Confirming the qualitative observation, the PLIC schemes produce comparable results in terms of both magnitude of nondimensional error and rate of convergence. This behavior was also observed by [56]. Even though the rate of convergence is similar with all the VOF modules, the magnitude of the nondimensional error is considerably larger with H&N + LHF compared to the PLIC-VOF techniques.

4.2 Single vortex test - 2D

After being introduced by [79], the single vortex test has been used by many researchers, e.g., [68], [54], [80], [9], [66], [33] and [36]. In the previous test, there was no fluid shear, therefore the geometry did not deform during its advection. In this test, we introduce shear into the velocity field in the form of a single vortex. A circle of radius 0.15 initially centered at point $(0.5, 0.75)$ inside a unit sized box is subjected to the following non-uniform velocity field which imposes a single vortex in the domain,

$$\begin{aligned} u &= \sin(2\pi y)\sin^2(\pi x)\cos\left(\frac{\pi t}{T}\right), \\ v &= -\sin(2\pi x)\sin^2(\pi y)\cos\left(\frac{\pi t}{T}\right). \end{aligned} \tag{16}$$

The velocity field is multiplied by the so-called Leveque cosine term $\cos(\pi t/T)$ where T is the period at which the flow returns to its initial state, [76]. This is merely a convenient way to establish temporal accuracy. In this test, $T = 8$ is used. The circle stretches and spirals about the center of the domain reaching maximum deformation at $t = T/2 = 4$, and the Leveque cosine term reverses the velocity field returning the deformed body back to its initial state at $t = T = 8$. The velocity values are averaged at the cell faces so that the discrete incompressibility is satisfied. The CFL number computed using the maximum velocity in the domain is 1.

Common use of the single vortex test among researchers is not surprising as it is a convenient yet challenging test to assess the ability of interface tracking methods in maintaining thin, elongated fluid filaments in a flow. In this test, these filaments are formed as a result of the vortex progressively stretching and wrapping the initial circular fluid body inward toward the vortex center. The duration of evolution from the initial configuration is controlled by the period T. Using large values for T indicates that the circle undergoes stretching for a long time, and the fluid filaments become thinner as more spirals are formed in the domain. Consequently, it becomes increasingly difficult for the interface tracking methods to bring the deformed body back to its initial state.

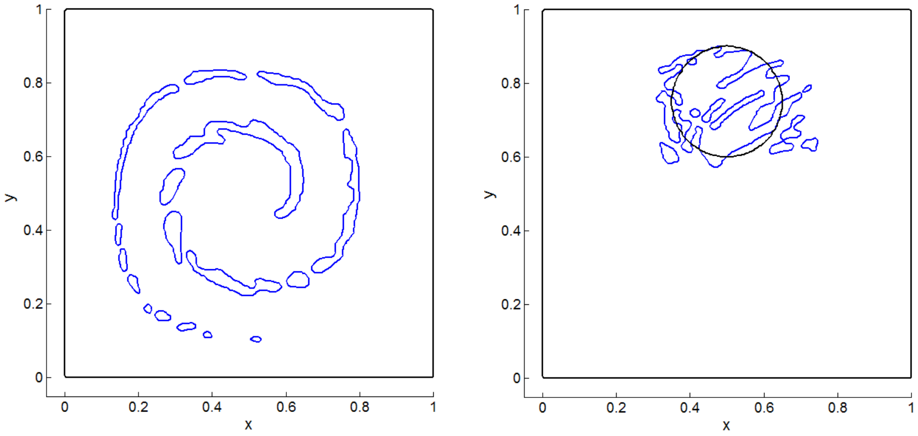

(a) $t = 4$ (b) $t = 8$

Figure 4: Single vortex test in 2D. Profile at maximum deformation ($t = 4$), and after full flow reversal ($t = 8$) using the H&N+LHF method. The grid is 128×128, and CFL=1.

Figure 4 shows results from the H&N+LHF method on a 128×128 grid. At maximum deformation we observe a large amount of spurious fragmentation and coalescence, and at the end of the test the method completely fails to capture the initial shape.

Figure 5 illustrates profiles at maximum deformation at $t = 4$ using four reconstruction methods with the COSMIC advection scheme on a 128×128 grid at CFL=1. Results indicate that as the fluid filament becomes thinner, fragmentation occurs at the tail of the deformed geometry where the curvature is high and the interface is somewhat under-resolved. On the other hand, at the head of the geometry where the curvature is also high, we observe coalescence which results in a *blobby* structure. Figure 5 shows that the performances of the four PLIC methods are qualitatively similar. The amount of fragmentation is largest with the Parker and Youngs' method (P&Y), and smallest with the ELVIRA method.

When the deformed geometry is brought back to its initial shape and location at $t = 8$, the four reconstruction methods produce also somewhat similar results, see Fig. 6. The profiles indicate a slight phase shift compared to the initial circle.

Mesh	LSG		ELVIRA		LSF	CVTNA	H&N+LHF
	COSMIC	EI-LE	COSMIC	EI-LE	EI-LE	PCFSC	
32^2	2.74×10^{-3} *1.97*	2.70×10^{-3} *1.96*	2.55×10^{-3} *1.97*	2.54×10^{-3} *1.97*	1.75×10^{-3} *1.91*	2.34×10^{-3} *2.12*	1.01×10^{-2} *0.94*
64^2	7.01×10^{-4} *1.84*	6.93×10^{-4} *1.87*	6.50×10^{-4} *2.11*	6.47×10^{-4} *2.16*	4.66×10^{-4} *2.19*	5.38×10^{-4} *2.03*	5.25×10^{-3} *1.09*
128^2	1.96×10^{-4}	1.89×10^{-4}	1.51×10^{-4}	1.45×10^{-4}	1.02×10^{-4}	1.31×10^{-4}	2.47×10^{-3}

Table 2: Error (12) for the 2D single vortex problem with $T = 2$. CFL is equal to 1. The results in the columns with the headers LSF/EI-LE and CVTNA/PCFSC are taken from [66] and [33], respectively. Rate of convergence (14) is written in italics between mesh entries.

Table 2 shows the geometrical error (12) from various VOF modules. To be able to compare our results with the literature, now we take $T = 2$. The data in the fifth column are taken from [66] as benchmark results. [66] use their iterative linear Least-Square Fit (LSF) reconstruction scheme in combination with the EI-LE advection. In this work, LSF was applied only in 2D, but later [55] extended the method to the three-dimensional space. Another set of results is shown in the sixth column taken from [33]. This work includes the implementation of the iterative Centroid-Vertex Triangle-Normal Averaging (CVTNA) for reconstruction, and the Piecewise-Constant Flux Surface Calculation (PCFSC) for unsplit advection. For

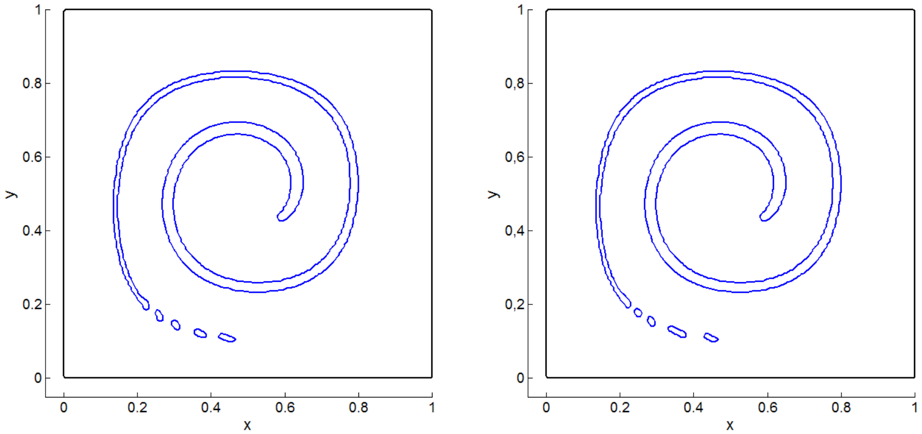

(a) LSG (b) MYC

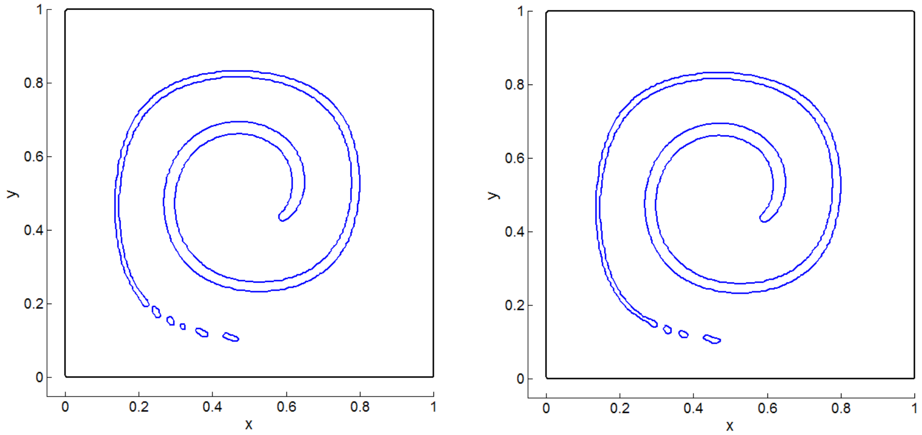

(c) P&Y (d) ELVIRA

Figure 5: Single vortex test in 2D. Profiles at maximum deformation ($t = 4$) using four reconstruction methods with the COSMIC advection scheme. The grid is 128×128, and CFL=1.

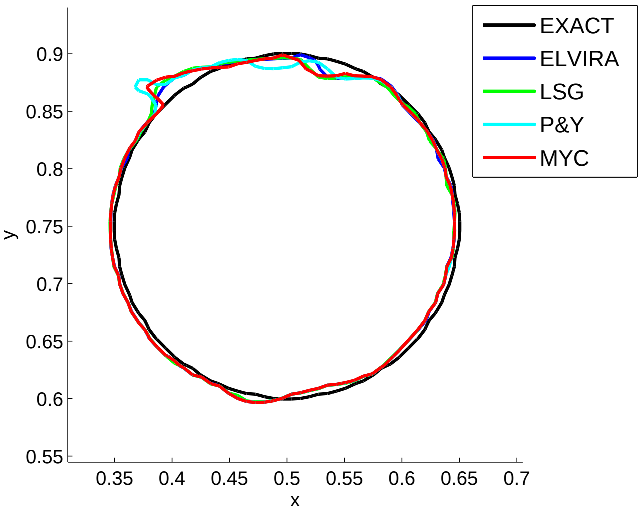

Figure 6: Single vortex test in 2D. Profiles at $t = T = 8$ from four reconstruction methods with the COSMIC advection scheme. The grid is 128×128, and CFL=1.

the same advection method EI-LE, the LSG scheme performs the worst compared to ELVIRA and LSF in terms of both magnitude of geometrical error and rate of convergence. However, the difference is modest considering the fact that LSG is the cheapest and least complex among its counterparts [81]. For the same reconstruction method, performances of the advection schemes COSMIC and EI-LE are close. Although not shown in the table, this test was performed with MACHO as well, and the results were similar to those from COSMIC. The first-order accuracy of the H&N + LHF method is confirmed once again.

4.3 Shearing flow - 3D

In the next test, introduced by [33] and later used by [82], a sphere of radius 0.15 and center $(0.5, 0.75, 0.25)$ in a domain of $1 \times 1 \times 2$ is immersed in a velocity field which is a combination of the single vortex in the $x - y$ plane prescribed by Eq. (16) with laminar pipe flow in the z-direction. The velocity field is stated by

$$\begin{aligned} u &= \sin(2\pi y)\sin^2(\pi x)\cos\left(\frac{\pi t}{T}\right), \\ v &= -\sin(2\pi x)\sin^2(\pi y)\cos\left(\frac{\pi t}{T}\right), \\ w &= -U_{\max}\left(1 - \frac{r}{R}\right)^2 \cos\left(\frac{\pi t}{T}\right) \end{aligned} \tag{17}$$

where $U_{\max} = 1.0$, $r = \sqrt{(x - x_0)^2 + (y - y_0)^2}$, $R = 0.5$, $x_0 = 0.5$ and $y_0 = 0.5$.

Figure 7 shows the results which are obtained on a $64 \times 64 \times 128$ uniform grid with a CFL number equal to 1. The LSG, MYC and ELVIRA schemes are used in combination with the MACHO advection scheme. In the plots, geometries in blue color illustrate results from the numerical methods, and spheres in red color at the bottom of the plots illustrate the initial geometry. Only the second half of the test is shown in several snapshots; from maximum deformation at $t = 3$ to full reversal of the flow at $t = 6$.

Analogous to the previous tests, H&N + LHF performs the worst amongst the VOF modules. With the other methods, we observe holes in the thin, deformed fluid sheets around the instant $t = 3$. Also, at the tail of the body, we observe spurious fragmentation. Comparing the PLIC schemes, ELVIRA shows the best qualitative performance around the instant of maximum deformation. We notice significant reduction in

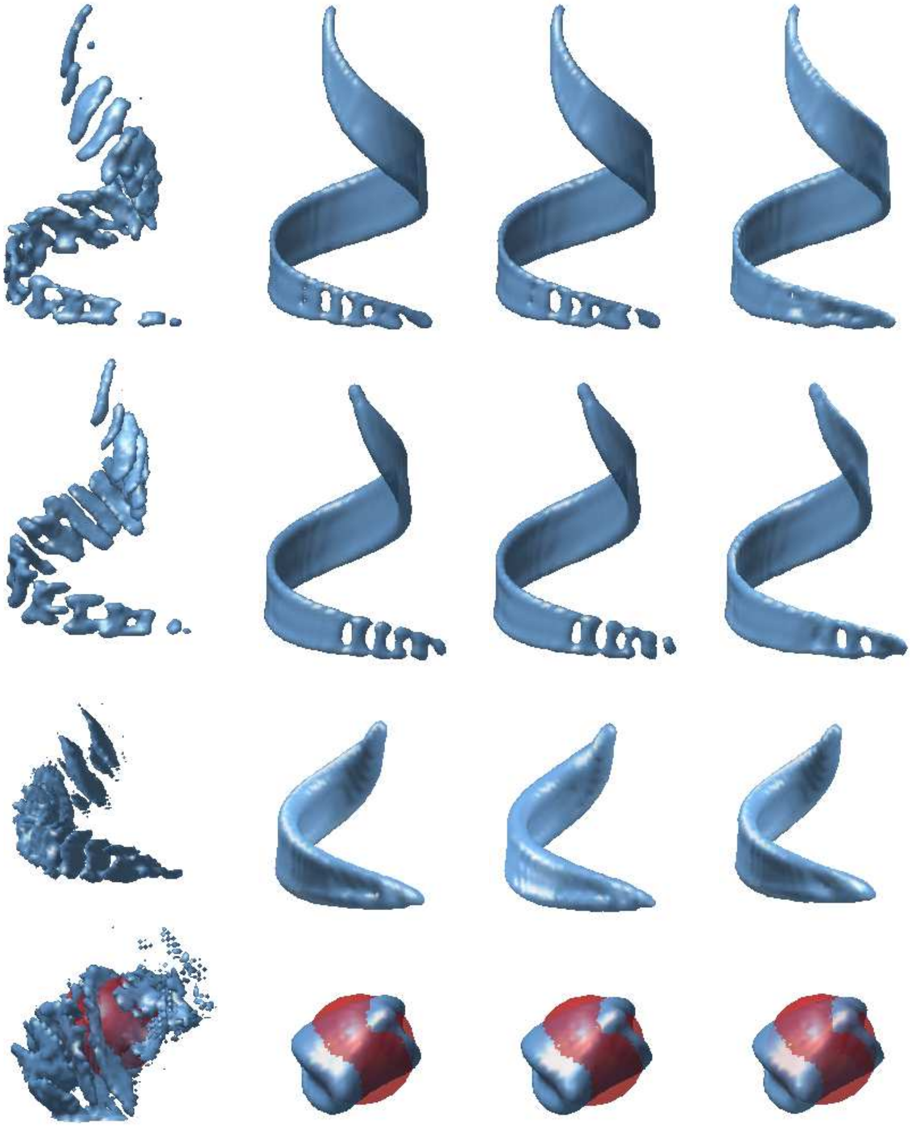

(a) H&N + LHF (b) MYC (c) LSG (d) ELVIRA

Figure 7: 3D reversible shearing flow test: a combination of single vortex flow and laminar pipe flow. Only the second half of the test is depicted through several snapshots taken at several instances from $t = 3$ (plots at the top) to $t = 6$ (plots at the bottom). Results are obtained on a $64 \times 64 \times 128$ uniform grid at CFL $= 1.0$. The PLIC methods are combined with the MACHO advection scheme. Geometries in blue color indicate numerical results, and spheres in red color in the plots at the bottom indicate the exact solution.

fragmentation at the tail, and less holes in the thin fluid sheets. However, the results from the PLIC-MACHO modules at the end of the test are almost indistinguishable.

Mesh	LSG		ELVIRA		CLC-CBIR	H&N+LHF
	MACHO	COSMIC	MACHO	COSMIC	FMFPA-3D	
$32\times32\times64$	1.20×10^{-2}	1.17×10^{-2}	1.16×10^{-2}	1.17×10^{-2}	9.95×10^{-3}	6.20×10^{-2}
	1.51	*1.51*	*1.53*	*1.52*	*1.61*	*1.07*
$64\times64\times128$	4.21×10^{-3}	4.10×10^{-3}	4.01×10^{-3}	3.97×10^{-3}	3.27×10^{-3}	2.95×10^{-2}
	1.45	*1.44*	*1.51*	*1.49*	*1.82*	*1.05*
$128\times128\times256$	1.54×10^{-3}	1.51×10^{-3}	1.41×10^{-3}	1.40×10^{-3}	9.27×10^{-4}	1.42×10^{-2}

Table 3: Error (12) for the 3D shearing flow test (single vortex in the $x-y$ plane with laminar pipe flow in the z-direction). CFL is equal to 1.0. The column with the header CLC-CBIR/FMFPA-3D shows data taken from [82] for comparison. Rate of convergence (14) is written in italics between mesh entries.

Table 3 shows the geometrical error (12). The data in the column with the header CLC-CBIR/FMFPA-3D is taken from [82] for comparison. This study includes the implementation of the coupled Conservative Level-Contour and Cubic-Bezier-based Interface Reconstruction (CLC-CBIR), and the Face-Matched Flux Polyhedra (FMFPA-3D) for unsplit advection in 3D. The first-order accuracy of the H&N + LHF method is obvious. Although the CLC-CBIR/FMFPA-3D combination of [82] outperforms the other PLIC-VOF modules, there is not a considerable difference in terms of both magnitude of geometrical error and rate of convergence. Analogous with the previous test, the performance of the advection schemes MACHO and COSMIC is similar for the same reconstruction method. Considering the reconstruction schemes, ELVIRA shows a slightly better performance than LSG in terms of magnitude of error, though both schemes have similar order of accuracy.

This and the previous numerical tests validate our VOF implementations as they compare favorably with the seminal literature works. Taking into account the steep increase in mathematical complexity and the large number of algorithmic tasks that come with the top-of-the-line contemporary VOF techniques, such as the CVTNA/PCFSC combination of [33] or the CLC-CBIR/FMFPA-3D combination of [82], we opted to implement techniques that result in a reasonable amount of decrease in accuracy for the sake of reduction in computational effort and mathematical complexity [81]. In the end, the results from the numerical tests proved to be consistent with this initial strategy.

4.4 Application example: Propagating Rienecker-Fenton waves

In the final test, we will assess the performance of the new VOF modules consisting of several reconstruction and advection schemes in a practical application. For this purpose, the VOF modules are incorporated into the CFD flow solver ComFLOW. We will generate Rienecker-Fenton waves [83] in shallow water in 2D, and monitor wave propagation throughout the domain. We particularly focus our attention on investigating the effect of various VOF modules on energy dissipation in these simulations. Two Rienecker-Fenton waves with the same period but different heights are generated, see Table 4. WAVE2 has a steepness of 2.0% and WAVE10 has a steepness of 10.8% which indicates strong nonlinear behavior in the flow. Both waves are started from rest, and within the first three periods, wave heights are gradually increased until full heights are reached.

Waves	*period* T(s)	*height* H(m)	*length* L(m)	*steepness* H/L(%)
WAVE2	4	0.5	24.7	2.0
WAVE10	4	3.0	27.6	10.8

Table 4: Characteristics of the Rienecker-Fenton waves.

The length of the domain in the direction of propagation is defined in such a way that both waves do not reach the end of the domain during the simulations. This procedure guarantees that there is no reflection in the computational domain, and hence the solution is not perturbed. The duration of the simulations should allow us to have a comprehensive picture regarding wave damping. Therefore, a stable wave system for a large number of wave periods is required. In this analysis, we performed simulations for 200 seconds to have a stable wave system for at least 18 consecutive wave lengths, and correspondingly a domain length of 2000 meters is considered sufficient taking the fastest propagating wave component into account. The water depth in all simulations is 10 meters. Three uniform grid resolutions are considered for the grid convergence study: $1m \times 1m$, $0.5m \times 0.5m$ and $0.25m \times 0.25m$.

Figures 8 and 9 show wave elevation as a function of the horizontal position at time $t = 200s$ on three uniform grid resolutions for WAVE2 and WAVE10, respectively. The first 500m of the full computational domain is plotted, since this part provides ample insight concerning the dissipation property of the VOF schemes. The results are obtained by using three PLIC algorithms with the MACHO advection scheme; the Mixed Youngs-centered (MYC) scheme of [55], the least squares gradient (LSG) technique by [54] and the efficient least squares VOF interface reconstruction algorithm (ELVIRA) by [56]. Also, the analytical results from the Rienecker-Fenton theory and the Hirt-Nichols' VOF with local height function (H&N + LHF) are plotted in the figures.

To analyze the results quantitatively, we will use two error definitions. The first error is the relative difference in wave height ε_H between the numerical results and the prescribed value for each wave given in Table 4. The second error is the relative shift ε_L between the numerical and analytical positions in the x-direction at which waves reach highest elevations. The expressions for ε_H and ε_L are given by

$$\varepsilon_H = \frac{|H_n - H|}{H} \times 100, \qquad \varepsilon_L = \frac{|x_{\eta_n} - x_{\eta_a}|}{L} \times 100. \tag{18}$$

Table 5 shows maximum ε_H and ε_L values in Figs. 8 and 9. The rate of error reduction as the grid is refined is obtained using (14) and written in italics and green color between mesh entries.

Waves	Resolution	MYC		ELVIRA		LSG		H&N+LHF	
		ε_H	ε_L	ε_H	ε_L	ε_H	ε_L	ε_H	ε_L
WAVE2	$1m\times1m$	30.5	12.9	27.2	12.9	29.5	12.7	48.9	8.9
		3.12	*0.70*	*3.04*	*0.72*	*2.47*	*0.64*	*1.78*	*0.36*
	$0.5m\times0.5m$	3.5	7.9	3.3	7.8	5.3	8.1	14.2	6.9
		0.37	*3.30*	*0.40*	*3.28*	*0.72*	*3.33*	*0.94*	*2.52*
	$0.25m\times0.25m$	2.7	0.8	2.5	0.8	3.2	0.8	7.4	1.2
WAVE10	$1m\times1m$	66.5	35.1	62.3	31.4	65.1	35.2	80.3	49.6
		1.12	*0.12*	*1.33*	*0.08*	*1.19*	*0.13*	*0.78*	*0.57*
	$0.5m\times0.5m$	30.5	32.2	24.7	29.7	28.4	32.1	46.7	33.3
		1.65	*2.08*	*1.59*	*2.28*	*1.64*	*2.30*	*0.73*	*1.87*
	$0.25m\times0.25m$	9.7	7.6	8.2	6.1	9.1	6.5	28.1	9.1

Table 5: ε_H (%) and ε_L (%) values computed by (18). Rate of convergence (14) is written in italics and green color between mesh entries. Results are shown for WAVE2 and WAVE10 using four VOF schemes on three uniform grid resolutions of $1m\times1m$, $0.5m\times0.5m$ and $0.25m\times0.25m$. The MYC, ELVIRA and LSG reconstruction methods are combined with the MACHO advection scheme.

For both WAVE2 and WAVE10 the results show that the resolution of $1m \times 1m$ is very insufficient, which is expected since this resolution corresponds to, for example, only 3 cells per wave wave height and 27 cells per wave length for WAVE10. On the finest grid with the resolution of $0.25m \times 0.25m$ all the VOF schemes show better performances

If we look at the ε_L values in Table 5, we see that the performance of H&N + LHF for both WAVE2 and WAVE10 is comparable to those of the PLIC-VOF schemes. For WAVE2 the ε_L value from H&N + LHF on the coarsest grid is 8.9% while the smallest ε_L value from the PLIC schemes is 12.7% produced by LSG. For the same wave on the finest grid H&N + LHF produces an ε_L value of 1.2% while the value from PLIC schemes is 0.8%. Although H&N + LHF initially starts with the smallest ε_L value on the coarsest

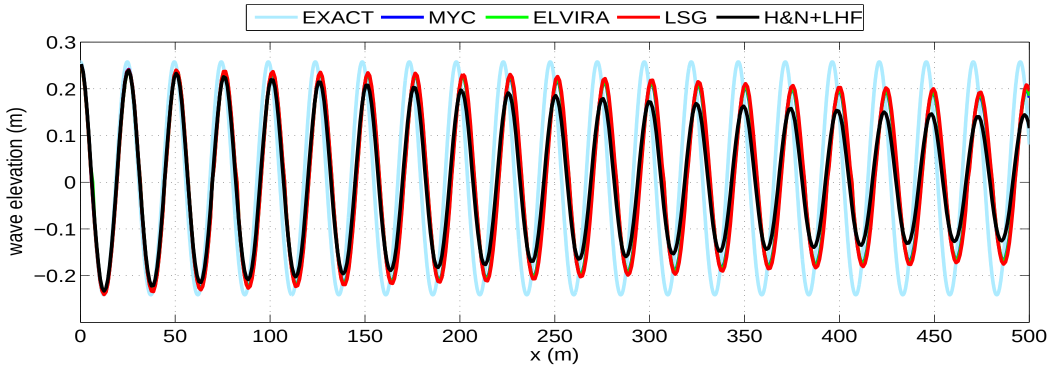

(a) Grid resolution is $\Delta x = \Delta z = 1m$

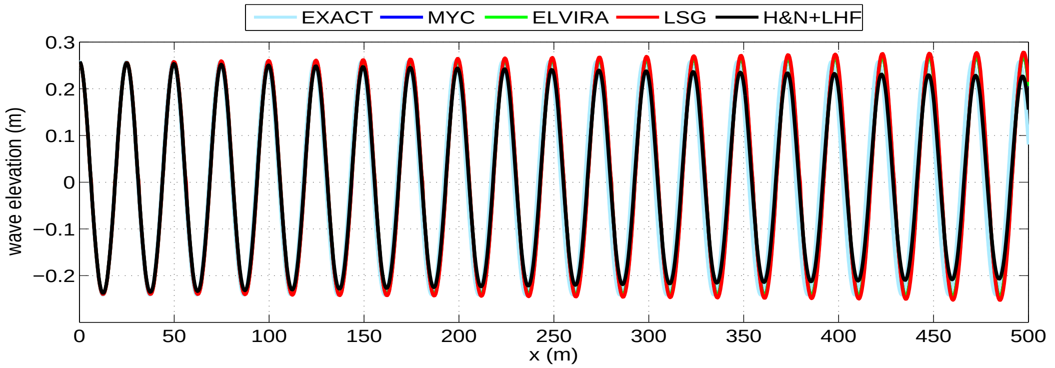

(b) Grid resolution is $\Delta x = \Delta z = 0.5m$

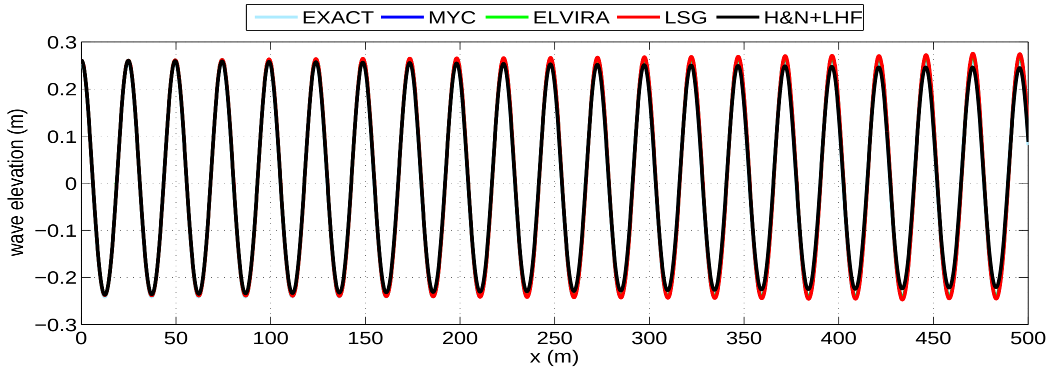

(c) Grid resolution is $\Delta x = \Delta z = 0.25m$

Figure 8: Wave elevations as a function of horizontal location at time $t = 200s$ for WAVE2. The MYC, ELVIRA and LSG reconstruction methods are combined with the MACHO advection scheme.

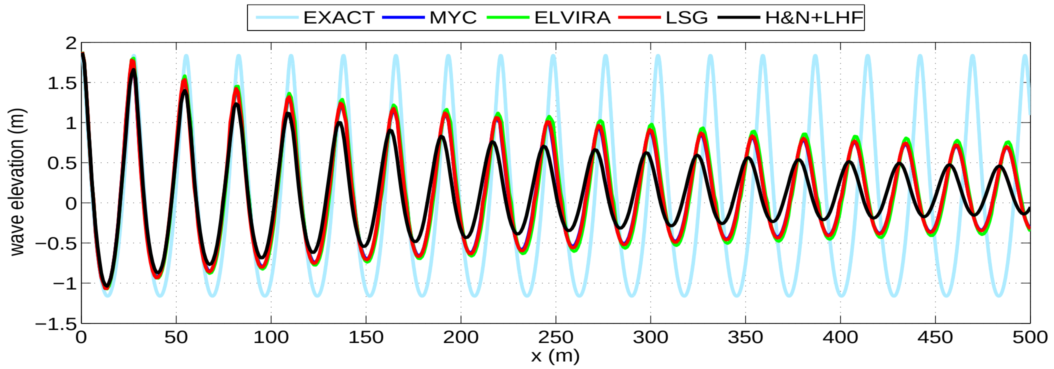

(a) Grid resolution is $\Delta x = \Delta z = 1m$

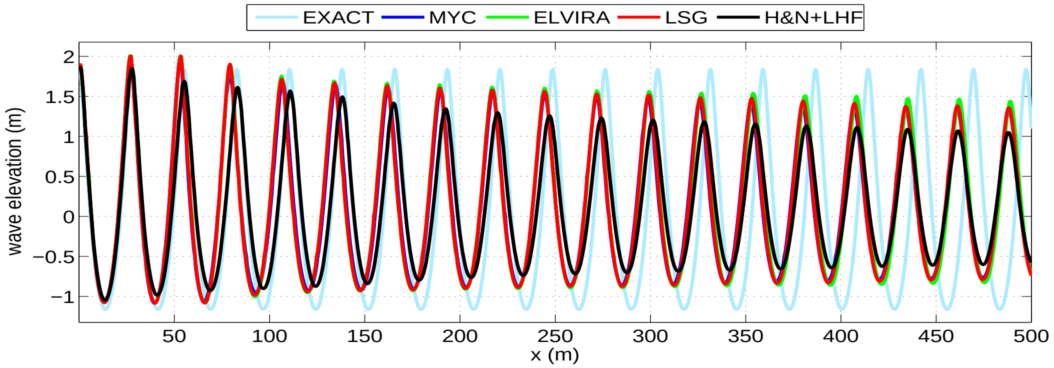

(b) Grid resolution is $\Delta x = \Delta z = 0.5m$

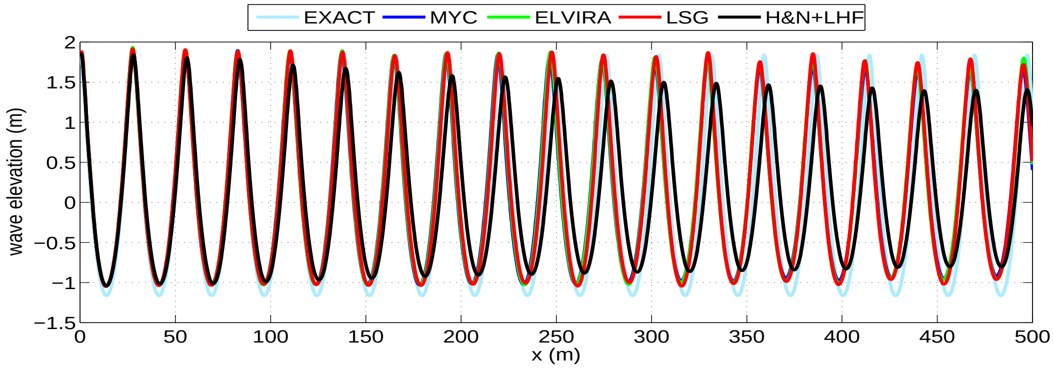

(c) Grid resolution is $\Delta x = \Delta z = 0.25m$

Figure 9: Wave elevations as a function of horizontal location at time $t = 200s$ for WAVE10. The MYC, ELVIRA and LSG reconstruction methods are combined with the MACHO advection scheme.

grid, its rate of convergence is somewhat poorer compared to PLIC methods, and it ends up with a larger but comparable error on the finest grid. For WAVE10 which is more challenging and more non-linear, H&N + LHF produces larger ε_L values on all the resolutions. On the finest grid the 9.1% error from H&N + LHF is larger than, but still comparable to, the 6.1% error from ELVIRA.

The values of ε_H in Table 5 depict, however, a different picture. On all the resolution levels the PLIC schemes demonstrate a clearly superior performance. For WAVE2 ELVIRA produces the smallest ε_H value of 27.2% on the coarsest grid while H&N + LHF produces 48.9%. On the finest grid this value reduces to 2.5% with ELVIRA and 7.4% with H&N + LHF. For WAVE10 ELVIRA is again the best performing method. On the resolution of $1m \times 1m$ the ε_H value from ELVIRA is 62.3% while that from H&N + LHF is 80.3%. As the grid is refined in two levels, the error from ELVIRA decreases at a rate of 1.33 and 1.59, while the error from H&N + LHF decreases at a rate of 0.78 and 0.73. On the finest grid the ε_H value from ELVIRA in only 8.2% while that from H&N + LHF is 28.1%.

For WAVE2 the wave signals obtained with the three PLIC methods are almost the same for all the three grid resolutions. For WAVE10 PLIC methods perform again very similarly. Both errors indicate that ELVIRA performs better compared to others but only very slightly.

Figure 10 illustrates the results to compare the performance of the advection methods. Here wave elevation as a function of the horizontal position is plotted at time $t = 200s$ on three uniform grid resolutions for WAVE10. The MACHO, EI-LE and COSMIC advection methods are used in combination with the ELVIRA reconstruction scheme. The results demonstrate that all the three advection methods resulted in almost the same profiles at the three grid resolutions. When these advection methods were combined with other PLIC reconstruction schemes, we again observed similar performances from the advection schemes but preferred not to put those results here for the sake of brevity. This observation is valid for WAVE2 as well.

5 Concluding remarks

Several PLIC-VOF methods have been implemented in the CFD tool ComFLOW, and their performances have been demonstrated in a number of test cases. In these tests the PLIC-VOF methods have also been compared to the original VOF implementation in COMFLOW, the H&N + LHF method. The test cases included a set of standard advection problems and an application example with Rienecker-Fenton waves. In the advection tests velocity fields are defined in such a way that advected fluid bodies return to their original shapes and locations at the end of the simulation. Therefore, the volume fraction distribution at the end of the simulation is expected to be equal to the original volume fraction distribution which can be considered as the exact solution. The difference between these two distributions gives an estimation of accuracy of a VOF method. In the application example with Rienecker-Fenton waves, spurious energy dissipation in the computational domain was monitored, which manifests itself as loss of wave height accompanied by phase shift. The results demonstrated that PLIC-VOF methods outperform the H&N + LHF method by a clear margin without increasing computational costs in a disproportionate manner. In the advection tests the PLIC-VOF methods showed a superior performance over the H&N + LHF method both qualitatively and quantitatively, and in simulations of Rienecker-Fenton waves a significant reduction in errors in terms of loss of wave height as well as phase shift was observed. It is possible to conclude that although the H&N + LHF method may be adequate to model low-steepness water waves, it has a limited ability to model more nonlinear waves which are actually interesting in practical applications.

The PLIC-VOF methods which were used in this work do not involve highly complex mathematical procedures with a large number of algorithmic tasks, and do not have strict limitations in stability. Therefore, difficulty in implementing these methods was modest. Although direction splitting advection is easier to implement than unsplit advection especially in 3D, it requires at least three interface reconstruction sweeps to complete a volume tracking update. To overcome this increase in computational cost, we opted to implement reconstruction techniques which have slightly lower accuracy compared to some of the contemporary PLIC schemes, but are considerably cheaper as well as easier to implement [81]. In the end this strategy allowed us to achieve a satisfying level of accuracy in an economical manner.

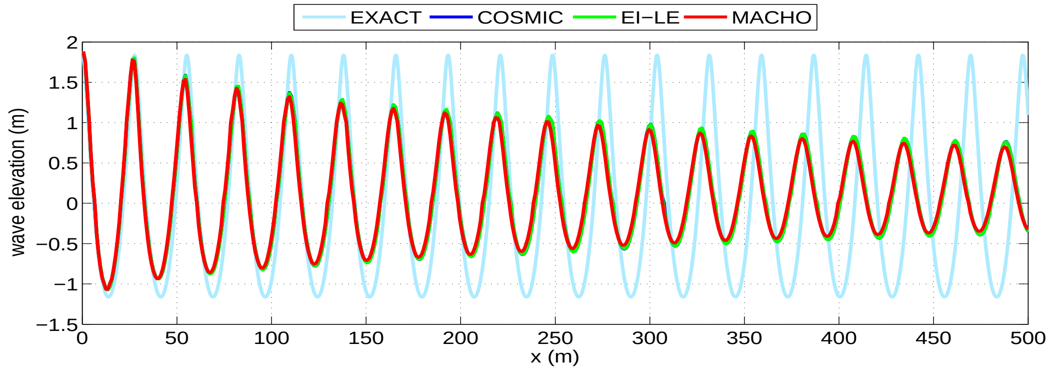

(a) Grid resolution is $\Delta x = \Delta z = 1m$

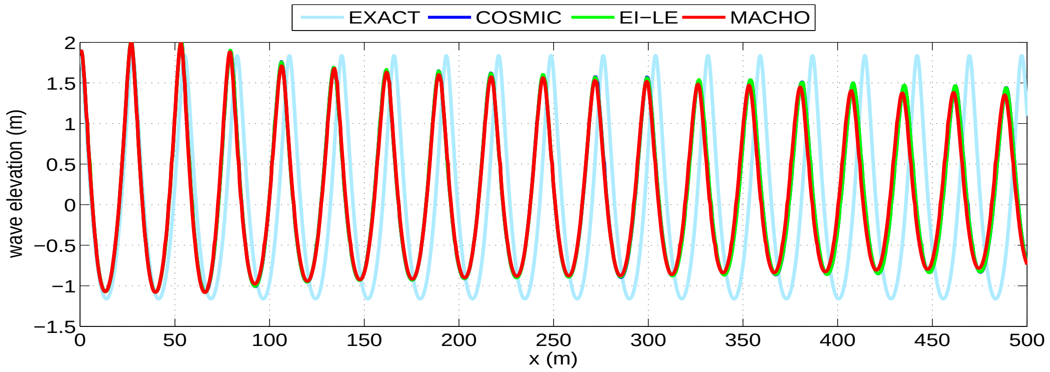

(b) Grid resolution is $\Delta x = \Delta z = 0.5m$

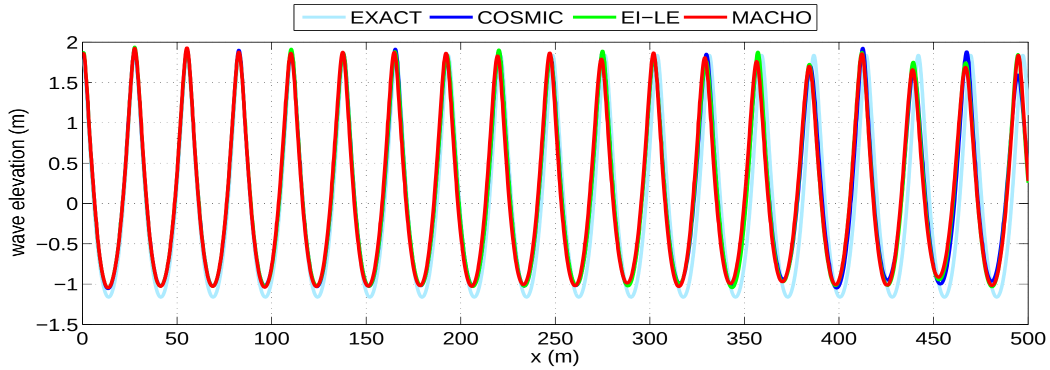

(c) Grid resolution is $\Delta x = \Delta z = 0.25m$

Figure 10: Wave elevations as a function of horizontal location for WAVE10. The COSMIC, EI-LE and MACHO advection schemes are combined with the ELVIRA reconstruction method.

Acknowledgment
This research is supported by the Dutch Technology Foundation STW, applied science division of NWO and the technology programma of the Ministry of Economic Affairs in The Netherlands (contracts GWI.6433 and 10475).

References

[1] G. Tryggvason, R. Scardovelli, and S. Zaleski. *Direct numerical simulations of gas-liquid multiphase flows.* Cambridge University Press, 2011.

[2] G.H. Yeoh and J. Tu. *Computational techniques for multiphase flows.* Butterworth-Heinemann, 2009.

[3] F.H. Harlow and J.E. Welch. Numerical calculation of time-dependent viscous incompressible flow of fluid with free surface. *Phys. Fluids*, 8:2182âĂŞ2189, 1965.

[4] J. Glimm, O.M. Bryan, R. Menikoff, and D. Sharp. Front tracking applied to Rayleigh-Taylor instability. *SIAM J. Sci. Stat. Comput.*, 7:230âĂŞ251, 1986.

[5] S. Chen, D.B. Johnson, and P.E. Raad. *The surface marker method*, pages 223–234. in: L.C. Wrobel and C.A. Brebbia (Eds.), Computational Modelling of Free and Moving Boundary Problems, vol. 1, Fluid flow, Walter de Gruyter & Co, 1991.

[6] S.O. Unverdi and G. Tryggvason. A front tracking method for viscous incompressible flow. *J. Comput. Phys.*, 100:25âĂŞ37, 1992.

[7] S. Osher and J. Sethian. Fronts propagating with curvature-dependent speed: algorithms based on Hamilton-Jacobi formulations. *J. Comput. Phys.*, 79:12âĂŞ49, 1988.

[8] M. Sussman, E. Fatemi, P. Smereka, and S. Osher. An improved level set method for incompressible two-phase flows. *Comput. Fluids*, 27:663âĂŞ680, 1998.

[9] D. Enright, R. Fedkiw, J. Ferziger, and I. Mitchell. A hybrid particle level set method for improved interface capturing. *J. Comput. Phys.*, 183:83–116, 2002.

[10] T. Yabe, F. Xiao, and T. Utsumi. The constrained interpolation profile (CIP) method for multi-phase analysis. *J. Comput. Phys.*, 169:556–593, 2001.

[11] H. Takewaki, A. Nishiguchi, and T. Yabe. Cubic interpolated pseudoparticle method (CIP) for solving hyperbolic-type equations. *J. Comput. Phys.*, 61:261–268, 1985.

[12] D. Jacqmin. Calculation of two-phase Navier-Stokes flows using phasefield modeling. *J. Comput. Phys.*, 155:96–127, 1999.

[13] H. Ding, P.D.M. Spelt, and C. Shu. Diffuse interface model for incompressible two-phase flows with large density ratios. *J. Comput. Phys.*, 226:2078–2095, 2007.

[14] P.R. Woodward and P. Colella. The numerical solution of two-dimensional fluid flow with strong shocks. *J. Comput. Phys.*, 54:115–173, 1984.

[15] D.J. Torres and J.U. Brackbill. The Point-Set method: front-tracking without connectivity. *J. Comput. Phys.*, 165:620–644, 2000.

[16] C.W. Hirt, J.L. Cook, and T.D. Butler. A Langrangian method for calculating the dynamics of an incompressible fluid with a free surface. *J. Comput. Phys.*, 5:103–124, 1970.

[17] M.J. Fritts and J.P. Boris. The Langrangian solution of transient problems in hydrodynamics using a triangular mesh. *J. Comput. Phys.*, 31:173–215, 1979.

[18] V. Dyadechko and M. Shashkov. Moment-of-fluid interface reconstruction. *Tech. Rep. LA-UR-05-7571, Los Alamos National Laboratory*, 2005.

[19] C.W. Hirt and B.D. Nichols. Volume of fluid (VOF) method for the dynamics of free boundaries. *J. Comput. Phys.*, 39:201–225, 1981.

[20] J.D. Ramshaw and J.A. Trapp. A numerical technique for low-speed homogeneous two-phase flow with sharp interfaces. *J. Comput. Phys.*, 21:438–453, 1976.

[21] N. Ashgriz and J.Y. Poo. FLAIR: Flux line-segment model for advection and interface reconstruction. *J. Comput. Phys.*, 93:449–468, 1991.

[22] B. Lafaurie, C. Nardone, R. Scardovelli, S. Zaleski, and G. Zanetti. Modelling merging and fragmentation in multiphase flows with SURFER. *J. Comput. Phys.*, 113:134–147, 1994.

[23] O. Ubbink. *Numerical prediction of two fluid systems with sharp interfaces.* PhD thesis, University of London, 1997.

[24] M.S. Darwish. A new high-resolution scheme based on the normalized variable formulation. *Numerical Heat Transfer, Part B*, 24:353–371, 1993.

[25] B.P. Leonard. The ULTIMATE conservative difference scheme applied to unsteady one-dimensional advection. *Comp. Meth. in Appl. Mech. and Eng.*, 88:17–74, 1991.

[26] H. Jasak, H.G. Weller, and A.D. Gosman. High resolution NVD differencing scheme for arbitrarily unstructured meshes. *Int. J. Numer. Meth. Fluids*, 31:431–449, 1999.

[27] G.R. Price. *A piecewise parabolic volume tracking method for the numerical simulation of interfacial flows*. PhD thesis, The University of Calgary, 2000.

[28] W.F. Noh and P.R. Woodward. *SLIC (Simple Line Interface Calculation)*, pages 330–340. in: A.I. van der Vooren and P.J. Zandbergen (Eds.), Lecture Notes in Physics, vol. 59, Springer-Verlag, New York, 1976.

[29] A.J. Chorin. Flame advection and propagation algorithms. *J. Comput. Phys.*, 35:1–11, 1980.

[30] D.L Youngs. *Time-dependent multi-material flow with large fluid distortion*, pages 273–285. in: K.W. Morton and M.J. Baines (Eds.), Numerical Methods for Fluid Dynamics, Academic Press, New York, 1982.

[31] P. Lötstedt. A front tracking method applied to burger's equation and two-phase porous flow. *J. Comput. Phys.*, 47:211–228, 1982.

[32] D.J. Benson. Volume of fluid interface reconstruction methods for multi-material problems. *Appl. Mech. Rev.*, 55:151–165, 2002.

[33] P. Liovic, M. Rudman, J-L. Liow, D. Lakehal, and D. Kothe. A 3D unsplit-advection volume tracking algorithm with planarity-preserving interface reconstruction. *Comput. Fluids*, 35:1011–1032, 2006.

[34] M. Sussman and E.G. Puckett. A coupled level set and volume-of-fluid method for computing 3D and axisymmtric incompressible two-phase flows. *J. Comput. Phys.*, 162:301–337, 2000.

[35] T. Ménard, S. Tanguy, and A. Berlemont. Coupling level set/VOF/ghost fluid methods: Validation and application to 3D simulation of the primary break-up of a liquid jet. *Int. J. Multiphas. Flow*, 33:510–524, 2007.

[36] M. Jemison, E. Loch, M. Sussman, M. Shashkov, M. Arienti, M. Ohta, and Y. Wang. A coupled level set-moment of fluid method for incompressible two-phase flows. *J. Sci. Comput.*, 54:454–491, 2013.

[37] R. Wemmenhove. *Numerical simulation of two-phase flow in offshore environments*. PhD thesis, University of Groningen, 2008.

[38] R. Wemmenhove, R. Luppes, A.E.P. Veldman, and T. Bunnik. Numerical simulation of hydrodynamic wave loading by a compressible two-phase flow method. *Comput. Fluids*, 114:218–231, 2015.

[39] A.E.P. Veldman and M.E.S. Vogels. Axisymmetric liquid sloshing under low gravity conditions. *Acta Astronaut.*, 11:641–649, 1984.

[40] J. Gerrits and A.E.P. Veldman. Dynamics of liquid-filled spacecraft. *J. Eng. Math.*, 45:21–38, 2003.

[41] A.E.P. Veldman, J. Gerrits, R. Luppes, J.A. Helder, and J.P.B. Vreeburg. The numerical simulation of liquid sloshing on board spacecraft. *J. Comput. Phys.*, 224:82–99, 2007.

[42] G.E. Loots, B. Hillen, and A.E.P. Veldman. The role of hemodynamics in the development of the outflow tract of the heart. *J. Eng. Math.*, 45:91–104, 2003.

[43] N.M. Maurits, G.E. Loots, and A.E.P. Veldman. The influence of vessel wall elasticity and peripheral resistance on the flow wave form: CFD model compared to in-vivo ultrasound measurements. *J. Biomech.*, 40(2):427–436, 2007.

[44] C. Nouri, R. Luppes, A.E.P. Veldman, J.A. Tuszynski, and R. Gordon. Rayleigh instability of the inverted one-cell amphibian embryo. *Phys. Biol.*, 5(1):article 010506, 2008.

[45] B. Brodtkorb. Prediction of wave-in-deck forces on fixed jacket-type structures based on CFD calculations. In *Proceedings of the 27th Int. Conf. on Ocean, Offshore and Arctic Eng. OMAE, June 15-20 2008, Estoril (Portugal), vol. 5*, pages 713–721, 2008.

[46] D.G. Danmeier, R.K.M. Seah, T. Finnigan, D. Roddier, A. Aubault, M. Vache, and J.T. Imamura. Validation of wave run-up calculation methods for a gravity based structure. In *Proceedings of the 27th Int. Conf. on Ocean, Offshore and Arctic Eng. OMAE, June 15-20 2008, Estoril (Portugal), vol. 6*, pages 265–274, 2008.

[47] B. Iwanowski, M. Lefranc, and R. Wemmenhove. CFD simulation of wave run-up on a semi-submersible and comparison with experiment. In *Proceedings of the 28th Int. Conf. on Ocean, Offshore and Arctic Eng. OMAE, May 31-June 5 2009, Honolulu (USA), vol. 1*, pages 19–29, 2009.

[48] B. Iwanowski, M. Lefranc, and R. Wemmenhove. Numerical simulation of sloshing in a tank, CFD calculations against model tests. In *Proceedings of the 28th Int. Conf. on Ocean, Offshore and Arctic Eng. OMAE, May 31-June 5 2009, Honolulu (USA), vol. 5*, pages 243–252, 2009.

[49] K.M.T. Kleefsman, G. Fekken, A.E.P. Veldman, B. Iwanowski, and B.A. Buchner. A Volume-of-Fluid based simulation method for wave impact problems. *J. Comput. Phys.*, 206:363–393, 2005.

[50] O. Lande and T.B. Johannessen. CFD analysis of deck impact in irregular waves: wave representation by transient wave groups. In *Proceedings of the 30th Int. Conf. on Ocean, Offshore and Arctic Eng. OMAE, June 19-24 2011, Rotterdam (Netherlands), vol. 7*, pages 287–295, 2011.

[51] A.E.P. Veldman, R. Luppes, T. Bunnik, R.H.M. Huijsmans, B. Duz, B. Iwanowski, and et.al. Extreme wave impact on offshore platforms and coastal constructions. In *Proceedings of the 30th Int. Conf. on Ocean, Offshore and Arctic Eng. OMAE, June 19-24 2011, Rotterdam (Netherlands), vol. 7*, pages 365–376, 2011.

[52] A.E.P. Veldman, R. Luppes, H.J.L. van der Heiden, P. van der Plas, B. Duz, and R.H.M. Huijsmans. Turbulence modeling, local grid refinement and absorbing boundary conditions for free-surface flow simulations in offshore applications. In *Proceedings of the 33rd Int. Conf. on Ocean, Offshore and Arctic Eng. OMAE, June 8-13 2014, California(USA), vol. 2, V002T08A076*, 2014.

[53] B.J. Parker and D.L. Youngs. Two and three dimensional Eulerian simulation of fluid flow with material interfaces. *Technical Report 01/92, UK Atomic Weapons Establishment*, 1992.

[54] W.J. Rider and D.B. Kothe. Reconstructing volume tracking. *J. Comput. Phys.*, 141:112–152, 1998.

[55] E. Aulisa, S. Manservisi, R. Scardovelli, and S. Zaleski. Interface reconstruction with least-squares fit and split advection in three-dimensional Cartesian geometry. *J. Comput. Phys.*, 225:2301–2319, 2007.

[56] J.E. Pilliod and E.G. Puckett. Second-order accurate volume-of-fluid algorithms for tracking material interfaces. *J. Comput. Phys.*, 199:465–502, 2004.

[57] A. Cervone, S. Manservisi, and R. Scardovelli. An optimal constrained approach for divergence-free velocity interpolation and multilevel VOF method. *Comput. Fluids*, 47:101–114, 2011.

[58] W.H. Press, S.A. Teukolsky, W.T. Vetterling, and B.P. Flannery. *Numerical recipes in Fortran 90.* Cambridge University Press, 1996.

[59] H.T. Ahn and M. Shashkov. Multi-material interface reconstruction on generalized polyhedral meshes. *Tech. Rep. LA-UR-07-0656, Los Alamos National Laboratory*, 2007.

[60] R. Scardovelli and S. Zaleski. Analytical relations connecting linear interfaces and volume fractions in rectangular grids. *J. Comput. Phys.*, 164:228–237, 2000.

[61] J. López and J. Hernández. Analytical and geometrical tools for 3D volume of fluid methods in general grids. *J. Comput. Phys.*, 227:5939–5948, 2008.

[62] S. Popinet. An accurate adaptive solver for surface-tension-driven interfacial flows. *J. Comput. Phys.*, 228:5838–5866, 2009.

[63] B.P. Leonard, A.P. Lock, and M.K. MacVean. Conservative explicit unrestricted-time-step multidimensional constancy-preserving advection schemes. *Mon. Weather Rev.*, 124:2588–2606, 1996.

[64] G. Strang. On the construction and comparison of difference schemes. *SIAM J. Numer. Anal.*, 5:506–517, 1968.

[65] S.P. van der Pijl, A. Segal, C. Vuik, and P. Wesseling. Computing three-dimensional two-phase flows with a mass-conserving level set method. *Comput. Visual. Sci.*, 11:221–235, 2008.

[66] R. Scardovelli and S. Zaleski. Interface reconstruction with least-square fit and split Eulerian-Langrangian advection. *Int. J. Numer. Meth. Fluids*, 41:251–274, 2003.

[67] D. Lörstdad and L. Fuchs. High-order surface tension VOF-model for 3D bubble flows with high density ratio. *J. Comput. Phys.*, 200:153–176, 2004.

[68] M. Rudman. Volume-tracking methods for interfacial flow calculations. *Int. J. Numer. Meth. Fluids*, 24:671–691, 1997.

[69] S-J. Lin and R.B. Rood. Multidimensional flux-form semi-Langrangian transport schemes. *Mon. Weather Rev.*, 124:2046–2070, 1996.

[70] G.D. Weymouth and D.K.-P. Yue. Conservative Volume-of-Fluid method for free-surface simulations on Cartesian-grids. *J. Comput. Phys.*, 229:2853–2865, 2010.

[71] S.J. Mosso, B.K. Swartz, D.B. Kothe, and S.P. Clancy. Recent enhancements of volume tracking algorithms for irregular grids. *Technical Report LA-CP-96-227, Los Alamos National Laboratory*, 1996.

[72] G.H. Miller and P. Colella. A conservative three-dimensional Eulerian method for coupled solid-fluid

shock capturing. *J. Comput. Phys.*, 183:26–82, 2002.

[73] J. López, J. Hernández, P. Gómez, and F. Faura. A volume of fluid method based on multidimensional advection and spline interface reconstruction. *J. Comput. Phys.*, 195:718–742, 2004.

[74] T. Marić, H. Marschall, and D. Bothe. vofoam – A geometrical Volume-of-Fluid algorithm on arbitrary unstructured meshes with local dynamic adaptive mesh refinement using OpenFOAM. arXiv preprint arXiv:1305.3417, available online (http://arxiv.org/abs/1305.3417), 2013.

[75] Z. Wang, J. Yang, and F. Stern. A new volume-of-fluid method with a constructed distance function on general structured grids. *J. Comput. Phys.*, 231:3703–3722, 2012.

[76] R. Leveque. High-resolution conservative algorithms for advection in incompressible flow. *SIAM J. Numer. Anal.*, 33:627–665, 1996.

[77] J. Gerrits. *Dynamics of liquid-filled spacecraft.* PhD thesis, University of Groningen, 2001.

[78] S.T. Zalesak. Fully multidimensional flux-corrected transport algorithms for fluids. *J. Comput. Phys.*, 31:335–362, 1979.

[79] J.B. Bell, P. Colella, and H.M. Glaz. A second-order projection method for the incompressible Navier-Stokes equations. *J. Comput. Phys.*, 85:257–283, 1989.

[80] D.J.E. Harvie and D.F. Fletcher. A new volume of fluid advection algorithm: The stream scheme. *J. Comput. Phys.*, 162:1–32, 2000.

[81] B. Düz. *Wave generation, propagation and absorption in CFD simulations of free surface flows.* PhD thesis, Delft University of Technology, The Netherlands, 2015.

[82] J. López, C. Zanzi, P. Gómez, F. Faura, and J. Hernández. A new volume of fluid method in three dimensions-Part 2: Piecewise-planar interface reconstruction with cubic-Bézier fit. *Int. J. Numer. Meth. Fluids*, 58:923–944, 2008.

[83] M.M. Rienecker and J.D. Fenton. A Fourier approximation method for steady water-waves. *J. Fluid Mech.*, 104:119–137, 1981.